



HAL
open science

Synchronization of the astronomical time scales in the Early Toarcian: A link between anoxia, carbon-cycle perturbation, mass extinction and volcanism

Fatima-Zahra Ait-Itto, Mathieu Martinez, Gregory Price, Abdellah Ait Addi

► **To cite this version:**

Fatima-Zahra Ait-Itto, Mathieu Martinez, Gregory Price, Abdellah Ait Addi. Synchronization of the astronomical time scales in the Early Toarcian: A link between anoxia, carbon-cycle perturbation, mass extinction and volcanism. *Earth and Planetary Science Letters*, 2018, 493, pp.1-11. 10.1016/j.epsl.2018.04.007 . insu-01777678

HAL Id: insu-01777678

<https://insu.hal.science/insu-01777678>

Submitted on 18 Jul 2019

HAL is a multi-disciplinary open access archive for the deposit and dissemination of scientific research documents, whether they are published or not. The documents may come from teaching and research institutions in France or abroad, or from public or private research centers.

L'archive ouverte pluridisciplinaire **HAL**, est destinée au dépôt et à la diffusion de documents scientifiques de niveau recherche, publiés ou non, émanant des établissements d'enseignement et de recherche français ou étrangers, des laboratoires publics ou privés.

1 **Synchronization of the astronomical time scales in the Early Toarcian: a link between**
2 **anoxia, carbon-cycle perturbation, mass extinction and volcanism**

3

4 Fatima-Zahra Ait-Itto ^{a,*}, Mathieu Martinez ^{b,c}, Gregory D. Price ^d, Abdellah Ait Addi ^a

5

6 ^a Cadi Ayyad University, Faculty of Sciences and Techniques, Geosciences and

7 Environmental research's Laboratory, P.O. Box 549, Marrakech, Morocco

8 ^b MARUM: Center for Marine Environmental Sciences, Universität Bremen, Leobenerstr.,

9 28359 Bremen, Germany.

10 ^c Univ Rennes, CNRS, Géosciences Rennes - UMR 6118, 35000 Rennes, France

11 ^d School of Geography, Earth and Environmental Sciences Plymouth University, Plymouth,

12 Devon PL4 8AA, UK

13

14 **Abstract**

15 The Late Pliensbachian-Early Toarcian is a pivotal time in the Mesozoic era, marked by

16 pronounced carbon-isotope excursions, biotic crises and major climatic and oceanographic

17 changes. Here we present new high-resolution carbon-isotope and magnetic-susceptibility

18 measurements from an expanded hemipelagic Late Pliensbachian-Early Toarcian section from

19 the Middle Atlas Basin (Morocco). Our new astronomical calibration allows the construction

20 of an orbital time scale based on the 100-kyr eccentricity cycle. The Early Toarcian

21 Polymorphum Zone contains 10 to 10.5 repetitions of the 100-kyr eccentricity both in the

22 carbon-isotope and the magnetic-susceptibility data, leading to an average duration of $1.00 \pm$

23 0.08 myr. We also show that the Late Pliensbachian-Early Toarcian global carbon-cycle

24 perturbation has an average duration of 0.24 ± 0.02 myr. These durations are comparable to

25 previous astrochronological time scales provided for this time interval in the most complete

26 sections of the Tethyan area, and longer than what has been provided in condensed sections.
27 Anchoring this framework on published radiometric ages and astrochronological time scales,
28 we estimate that the carbon-cycle perturbation of the Late Pliensbachian-Early Toarcian
29 corresponds with the early phase of the Karoo and Chonke Aike large igneous provinces.
30 Likewise, our new age constraints confirm that the Toarcian oceanic anoxic event is
31 synchronous to the main phase of the Ferrar volcanic activity. Thus, these successive and short
32 phases of the volcanic activity may have been at the origin of the successive phases of the mass
33 extinctions observed in marine biotas in the Pliensbachian and Toarcian times.

34 **Keywords:**

35 Astrochronology; Toarcian; carbon cycle; Middle Atlas; oceanic anoxic events
36

37 **1. Introduction**

38 The Early Toarcian (184.15 – 174.1 Ma) was a time of global warming events (Dera et al.,
39 2011), mass extinctions (Little and Benton, 1995), and pronounced negative carbon-isotope
40 excursions recorded in marine carbonates and organic matter, brachiopods, biomarkers and
41 fossil wood (Hesselbo et al., 2007; Suan et al., 2008a; Ait-Itto et al., 2017). These events
42 coincide with carbonate production demises (Bassoulet and Baudin, 1994; Wilmsen and
43 Neuweiler, 2008) and widespread oceanic anoxia (Jenkyns, 1988; Hesselbo et al., 2007).

44 Although large amounts of data have been produced, the timing and rhythms of the
45 environmental perturbations are still debated, leading to controversies on the mechanisms at the
46 onset of the climatic changes in the Early Toarcian (e.g. Kemp et al., 2005; Suan et al., 2008b).
47 For instance, Martinez et al (2017) assess the duration of Pliensbachian-Toarcian event (P-To
48 event) at 0.18 to 0.27 myr, while in the Peniche section (Lusitanian Basin, Portugal) the duration
49 of this event is evaluated as 0.05 myr (Suan et al., 2008b). Similarly, the estimates of duration
50 of the Polymorphum Zone vary from 90 kyr to 1.15 myr (Matiolli and Pittet, 2004; Suan et al.,

51 2008b, Boulila et al., 2014; Huang and Hesselbo, 2014; Ruebsam et al., 2014; Martinez et al.,
52 2017). The main reason of these differences is the occurrence of four discontinuity events
53 identified by correlations of $\delta^{13}\text{C}$ and sedimentological features throughout the Tethyan
54 margins, which are due to changes in the sea level observed in the earliest Toarcian (Pittet et
55 al., 2014). The section studied here in Issouka, Morocco, is expanded compared to the
56 sedimentary series from the northern Tethyan margin. It provides the opportunity to fill the gap
57 in the time scale of the Toarcian Stage and to establish a detailed chronology of the succession
58 of the environmental disturbances occurring in the Early Toarcian.

59

60 **2. Geological setting**

61 The geological history of Morocco was influenced by two important events, starting in the early
62 Mesozoic with the opening of the north Atlantic and western Tethys and the collision of Africa
63 and Europe during the middle Cenozoic (Michard, 1976). These events led to the formation of
64 fault-bounded basins, which are made up of several smaller depocenters, separated by
65 synsedimentary highs (Studer and Du Dresnay, 1980). The Middle Atlas is one of these small
66 fault-bounded basins (Fig. 1). It constitutes a part of a Meso-Cenozoic intracontinental chain,
67 namely the Moroccan Atlas (Michard, 1976). The Middle Atlas of Morocco is structurally
68 dominated by four NE–SW trending anticlines and is mainly constituted of Lower and Middle
69 Jurassic formations (Du Dresnay, 1971). The basin is bounded by the Saïs Plain and the front
70 of the Rifian Nappes in the North, by the Guercif Basin in the northeast, by the Moulouya Plain
71 to the southeast, and by the Hercynian Central Massif in the West.

72 The Middle Atlas Basin is deep in the center and shallows towards the northern and
73 southern basin margins (Du Dresnay, 1971). The study area during the Early Toarcian was
74 located at a palaeolatitude of $\sim 20^\circ\text{N}$ (Bassoulet et al., 1993) (Fig. 1A). The sedimentary
75 evolution and palaeogeographic differentiation is controlled by tectonic activity, combined with

76 the rate of sedimentation and global eustatic variations (Wilmsen and Neuweiler, 2008). The
77 rapid transition from shallow marine carbonates to hemipelagic marls has been taken to reflect
78 a major deepening phase across the entire Middle and High Atlas area (Wilmsen and Neuweiler,
79 2008). The Pliensbachian–Toarcian transition coincides with a dislocation of the Lower
80 Jurassic carbonate platform (Lachkar et al., 2009; Ait Addi and Chafiki, 2013) with Toarcian
81 deposits dominated by marls lying upon Upper Pliensbachian shallow marine limestones and
82 calcareous marls. This drowning episode is linked to the eustatic sea-level rise of the Early
83 Toarcian described in Europe and Africa (e.g. Hallam, 1997).

84 The biostratigraphy in the Middle Atlas has been established with ammonites (El
85 Hammichi et al., 2008) with further biostratigraphic data provided by benthic foraminifera
86 (Bejjaji et al., 2010). The ammonite zonation in the Issouka section is based on the
87 Mediterranean zonation. Notably, the ammonites *Emaciatoceras emaciatum* of the Emaciatum
88 Zone, *Dactyloceras polymorphum* of the Toarcian Polymorphum Zone and *Hildaites* in the
89 Semicelatum Zone have been identified (e.g. El Hammichi et al., 2008). Furthermore, the
90 occurrence of the benthic foraminifera *Lenticulina sublaevis* in the Issouka section is correlated
91 by Bejjaji et al. (2010) to the Emaciatum ammonite zone of the Pliensbachian, whilst
92 *Lenticulina bochari* and *Lenticulina toarcense* are correlated with the Toarcian Polymorphum
93 Zone and *Lenticulina obonensis* with the Serpentinus Zone.

94 The Issouka section is situated near the village of Issouka, ~25 km southwest of
95 Immouzer Marmoucha, in the Middle Atlas (N33° 26' 55.56"; W4° 20' 33.83"; Fig. 1). The
96 section begins with centimeter thick limestone–marl alternations (Fig. 2). The limestone beds
97 contain a rich ammonite fauna, with also belemnites, echinoids and brachiopods. Foraminifera
98 suggested a Late Pliensbachian age (Bejjaji et al., 2010; Fig. 2A). The early Toarcian succession
99 starts with green marls and marl–limestone alternations, rich in foraminifera, belemnites,

100 echinoids and gastropods. The Toarcian deposits are generally hemipelagic and correspond to
101 deep marine environments (Bejjaji et al., 2010; Fig. 2B).

102

103 **3. Material and methods**

104 A total of 430 bulk-rock samples were collected with an even sample distance of 10 cm in the
105 Issouka section. The samples were recovered from up to 15 cm below the surface, to minimize
106 the effects of surface weathering. The sampled interval encompasses the end of the
107 Pliensbachian Stage to the lowermost part of the Levisoni ammonite Zone. Such a range allows
108 the Polymorphum Zone to be entirely sampled. The bulk-rock samples were then powdered
109 using a metal ring grinder and analyzed for stable isotopes, magnetic susceptibility and calcium
110 carbonate contents.

111

112 **3.1. Carbon isotopes**

113 A total of 430 samples were analyzed for stable isotopes at the University of Plymouth. Using
114 200 to 300 micrograms of carbonate, stable isotope data were generated on a VG Optima mass
115 spectrometer with a Gilson autosampler. Isotope ratios were calibrated using NBS19 standards
116 and are given in δ notation relative to the Vienna Pee Dee Belemnite (VPDB). Reproducibility
117 was generally better than 0.1 ‰ for samples and standard material.

118

119 **3.2. Magnetic susceptibility**

120 The magnetic susceptibility (MS) of the 430 powdered samples was measured with a
121 Kappabridge KLY-3. The samples are placed in small plastic cubes of 10 cm³ and then
122 introduced inside the instrument using the “pick-up” unit. We measured the cube empty and
123 then with samples for blank correction. The blank-corrected MS values are normalized to their
124 mass and volume. The resulting values are reported as mass-specific MS (m³.kg⁻¹).

125

126 **3.3. Calcium carbonate content**

127 The samples were analyzed for their calcium carbonate content using a Bernard calcimeter at
128 the Geosciences and Environment Laboratory, Cadi Ayyad University. The values are given
129 with a precision between 1 and 5% (Lamas et al., 2005).

130

131 **3.4. Spectral analysis**

132 Prior to spectral analysis, the long-term trend of both series was measured and subtracted from
133 the series to ensure stationarity. The detrend procedures removed the high powers in the
134 frequencies close to 0, while not creating new spectral peaks in the low frequencies (see
135 Vaughan et al., 2015). Best-fit linear trend and LOWESS smoothing curves (Cleveland et al.,
136 1979) were applied. The exact coefficients depend on each of the series and are detailed in the
137 results. Following the removal of this long-term trend, the multi-taper spectral analyses, using
138 three 2π prolate tapers (2π -MTM) with robust red-noise modelling (Mann and Lees, 1996)
139 modified in Meyers (2014) were applied to evaluate lithological cycles as a possible record of
140 astronomically forced sedimentation following the LOWSPEC approach (Meyers, 2012). The
141 significance levels were then calculated assuming a chi-square distribution of the spectral
142 background. We used the time-frequency weighted fast Fourier transforms (T-F WFFT;
143 Martinez et al., 2015) to characterize the evolution of the periods through the sedimentary
144 series. Taner low-pass and band-pass filters (Taner, 2003) were then applied to isolate each
145 signal interpreted as an orbital forcing and calculate the duration of the Polymorphum Zone by
146 cycle counting. Orbital tuning procedures are then used to anchor the sedimentary cycles to
147 their corresponding orbital periods, allowing depth-time conversions to be done. Durations are
148 then estimated by calculating the difference of relative ages. Error margins of each of the time

149 intervals include the difference between the average and the calculated durations and the
150 uncertainty in the orbital frequencies.

151

152 **4. Results**

153 **4.1. Carbonate carbon isotopes**

154 The carbon-isotope profile of the Issouka section shows relatively high values in the
155 Pliensbachian part of the section, ranging from +1.7‰ to +2.7‰ (Fig. 3A). From 5 m to 5.6 m,
156 the $\delta^{13}\text{C}$ decreases from 2.5‰ to -0.6‰. This abrupt decrease of 3‰ in the $\delta^{13}\text{C}$ observed at
157 the base of the Toarcian is related to the Pliensbachian-Toarcian event (P-To event; Suan et al.,
158 2008a; Ait-Itto et al., 2017). The $\delta^{13}\text{C}$ values then remain low from 5 m to 23 m. In this interval,
159 the values show gentle fluctuations from 5 to 17 m. At 17 m, the $\delta^{13}\text{C}$ abruptly increase by 1‰
160 before they gently decrease until 23 m to -2‰. The values then progressively increase from 23
161 m to 30 m, changing from -2‰ to 1‰. Above 30 m to the top of the section, the values slightly
162 increase from 1 to 2‰.

163 **4.2. Magnetic susceptibility**

164 The magnetic susceptibility curve (Fig. 3E) firstly shows from the base of the series to level 5.1
165 m low values, ranging from 9.65×10^{-9} to $3.15 \times 10^{-8} \text{ m}^3 \cdot \text{kg}^{-1}$. This interval corresponds to the
166 limestone-dominated part of the formation of Pliensbachian age. From 5.2 m to the top of the
167 series, MS values increase with an average value $1.04 \times 10^{-7} \text{ m}^3 \cdot \text{kg}^{-1}$. The interval from 27 m to
168 35 m shows lower values of the MS in a more carbonated interval. Calcium carbonate content
169 and MS values display a strong inverse correlation ($r = -0.91$, Fig. 4), indicating that the
170 lithology mainly controls the MS variations.

171 **4.3. Calcium carbonate content**

172 The carbonate content series (Fig. 3D) firstly show high values (>80% on average) from the
173 base of the series to 5.1 m, in the interval of the limestone beds of the Pliensbachian. From 5.2

174 m to 8.4 m, the values rapidly decrease from 91% to 8.6%. From 5.2 m to 18 m, the CaCO₃
175 values remain low with average values around 22%. The transition between the first to the
176 second interval is more progressive than observed in the $\delta^{13}\text{C}$ series (Fig. 3A). From 18 m to
177 42.9 m CaCO₃ series show high-amplitude cycles and high-frequency fluctuations from 60%
178 and 20% linked to the limestone-marl alternations (Fig. 3D).

179 **4.4. Spectral analyses**

180 **4.4.1. Carbon-isotope signal**

181 The $\delta^{13}\text{C}$ shows a rapid decrease at 5.2 m, and a rapid increase at 16.6 m (Fig. 3A). The series
182 was stationarized using a best-fit linear trend from 0 to 5.1 m, a LOWESS regression with a
183 coefficient of 0.6 from 5.2 to 16.5 m and a LOWESS regression with a coefficient of 0.3 from
184 16.6 to 42.9 m. The LOWESS coefficients have been chosen in such a way that they
185 approximatively cover the same length of the section (i.e. ~7 m on average), which represents
186 *ca.* 20% of the Toarcian part. This choice decreased the high powers at frequencies near 0,
187 while not creating spurious spectral peaks in the low frequencies (Vaughan et al., 2015). The
188 three subseries were then standardized (average = 0, standard deviation = 1) and stacked. Two
189 points at 11.7 m and 12 m showing outstandingly low values when detrending may bias the
190 spectrum in the high frequencies and have been removed from the series before detrending. The
191 evolutive spectrum of the $\delta^{13}\text{C}$ series shows a high-power spectral band in the low frequencies
192 evolving having a period of 4.1 to 4.2 m from the base of the series to level 24 m (Fig. 3C). The
193 period of this band then decreases to 3 m, from level 24 m to level 31 m, and stabilizes at 3 m
194 from level 31 m to the top of the series. These changes in the period of the ~4-m peak likely
195 reflects variations in the sedimentation rate. These distort the sedimentary record of the orbital
196 cycles by decreasing the *p*-value of the low frequency and flattening the spectrum at high
197 frequencies (Weedon, 2003; Kemp, 2016; Martinez et al., 2016). We thus decided to analyze
198 the frequency content of two sub-intervals of the series in which variations in the sedimentation

199 rate are limited. The range of each of the sub-intervals is given in Fig. 3C. We compared the
200 frequencies of the carbon isotopes in each interval with the orbital frequencies calculated for
201 the Toarcian (Waltham, 2015), using the average spectral misfit (ASM; Meyers and Sageman,
202 2007). The ASM method compares the sedimentary frequencies converted into time to the
203 orbital frequencies and provides a quantitative assessment on the most likely sedimentation rate
204 in each sub-interval (see supplementary materials).

205 Spectra of Interval 1, from levels 0 to 31 m, show significant periods above the 99%
206 confidence level (CL) at 4.2 m (frequency: $0.2404 \text{ cycles.m}^{-1}$), and above the 95% CL at 1.2 m
207 (frequency: $0.8013 \text{ cycles.m}^{-1}$), 0.83 m (frequency: $1.202 \text{ cycles.m}^{-1}$), and 0.31 m (Fig. 5A, C).
208 Spectra of Interval 2, from levels 24 m to the top of the series show significant peaks above the
209 95% CL at 3.2 m (frequency: $0.3158 \text{ cycles.m}^{-1}$), 0.63 m ($1.579 \text{ cycles.m}^{-1}$) and 0.33 m (Fig.
210 5B, D).

211 As noted above, various astrochronological frameworks estimate the duration of the
212 Polymorphum Zone from 0.09 myr to 1.15 myr (Mattioli and Pittet, 2004; Suan et al., 2008b;
213 Huang and Hesselbo, 2014; Boulila et al., 2014; Martinez et al., 2017; Boulila and Hinnov,
214 2017), implying a sedimentation rate varying from 400 m/myr to 31 m/myr. When converting
215 m-cycles to time-cycles, the peaks at ~0.3 m have periods below the Milankovitch band
216 whatever the sedimentation rate considered, so were excluded from the ASM analysis. Testing
217 ASM over 500 sedimentation rates ranging from 0.4 cm/kyr to 40 cm/kyr leads to a most likely
218 sedimentation rate of 3.9 cm/kyr (39 m/myr) in Interval 1, and to a most likely sedimentation
219 rate of 3.2 cm/kyr (32 m/myr) in Interval 2 (Fig. 5E, F). The H₀-significance level at the most
220 likely sedimentation rate is below the critical significance level below which we can consider
221 without ambiguity these spectra reflect an orbital forcing. In Interval 1, peaks at 4.2 m, 1.2 m
222 and 0.83 m are respectively due to the 100-kyr eccentricity, the obliquity and the precession
223 cycles. Notice that the peak of 1.2 m leads to an obliquity period which is shorter than expected

224 in the theory (here 29.4 kyr vs. 37.5 kyr in Waltham, 2015). In Interval 2, peaks at 3.2 m and
225 0.63 m are respectively due to the 100-kyr eccentricity and the precession cycles. In addition,
226 the peak at 0.33 m has a mean period of 10 kyr, which corresponds to the semi-precession, the
227 first harmonic of the precession (Berger et al., 2006).

228 The evolutive spectral analysis indicates the 100-kyr cycle is the most continuous
229 throughout the studied series (Fig. 3C). We filtered the 100-kyr eccentricity recorded in the
230 $\delta^{13}\text{C}$ series and used it as target cycle for calibrating the series in time. We filtered the 100-kyr
231 cycle using a Taner low-pass filter with a frequency cut of 0.3953 cycles.m⁻¹ and a roll-off rate
232 of 10³⁶. The output filter indicates that the Polymorphum Zone contains 10 repetitions of the
233 100-kyr eccentricity cycle (Fig. 3B).

234

235 **4.4.2. Magnetic susceptibility**

236 The MS series is marked by a rapid increase of values from 5.0 m to 6.8 m. The trend of the
237 series is then gentler. The series was stationarized using a best-fit linear regression from 0 to
238 5.2 m and a LOWESS smoothing with a coefficient of 0.2 in the remainder of the series, which
239 represents 7.5 m of the section. The two subseries were then standardized (average = 0, standard
240 deviation = 1) and stacked. The evolutive spectrum of the MS series shows a band in the low
241 frequencies evolving from 3.1 m to 3.7 m in the lower part of the series, from the base of the
242 series to level 20 m (Fig. 3G). Then, this period decreases to 2.9 m from level 26 m to the top
243 of the series. 2π -MTM spectra have been generated from Interval 1 (from the base of the series
244 to level 26 m), and from Interval 2 (from 21 m to the top of the series) (Fig. 6). Spectra of
245 Interval 1 show spectral peaks over the 99% CL at 3.3 m and 0.38 m, and peaks over the 95%
246 CL at 0.81 m and 0.23 m (Fig. 6A, C). Spectra of Interval 2 show peaks over the 99% CL at 2.9
247 m, 2.0 m, 0.27 m and 0.22 m, and a peak exceeding the 95% CL at 1.0 m (Fig. 6B, D).

248 Assuming from ASM applied on the $\delta^{13}\text{C}$ spectra that Interval 1 has a mean
249 sedimentation rate of 39 m/myr, the peaks of 3.3 m, 0.81 m and 0.38 m are attributed to the
250 100-kyr eccentricity, the precession and the semi-precession, respectively. Assuming from
251 ASM that Interval 2 has a mean sedimentation rate of 32 m/myr, the peak of 2.9 m, 1.0 m and
252 0.27 m are respectively attributed to the 100-kyr eccentricity, the obliquity and the semi-
253 precession (Fig. 6).

254 In Interval 1, the period of the 100-kyr cycle is lower in the MS series than in the $\delta^{13}\text{C}$.
255 On the evolutive spectral analyses, this is particularly obvious in the first 10 m of the series,
256 when the lithology evolves from the limestones of the Pliensbachian to the marls of the Toarcian
257 (Fig. 3). The 100-kyr eccentricity recorded in the MS series was isolated using a Taner low-
258 pass filter with a frequency cut of $0.4070 \text{ cycles.m}^{-1}$ and a roll-off rate of 10^{36} (Fig. 3). The
259 output filter indicates that the Polymorphum Zone clearly contains ~ 10.5 repetitions of the 100-
260 kyr eccentricity cycle compared to the 10 repetitions observed in the $\delta^{13}\text{C}$ (Fig. 3).

261

262 **5. Discussion**

263 **5.1. Astrochronology of the the Polymorphum Zone**

264 The $\delta^{13}\text{C}$ and the MS signals both display 12 complete short eccentricity cycles along the
265 studied section. In the astronomical models computed for the last 20 myr (Laskar et al., 2004),
266 the average duration of 12 consecutive short eccentricity cycles is $1149 \pm 63 \text{ kyr}$ (2σ), so that
267 the average duration of a short eccentricity cycle $95.8 \pm 5.2 \text{ kyr}$ (2σ). Assuming a constant
268 sedimentation rate between two successive anchor points of the 100-kyr cycle obtained from
269 the filters of the $\delta^{13}\text{C}$ and the MS signals, the durations calculated of the Polymorphum Zone
270 range from 0.97 myr with the $\delta^{13}\text{C}$ signal, to 1.02 myr with the MS signal. In the spectra of the
271 untuned series, the period of the 100-kyr cycle is longer in the $\delta^{13}\text{C}$ than in the MS (Figs. 3, 5,
272 6). The difference is particularly noticeable in the first 10 m (Fig. 3). Below level 5 m, the filter

273 of 100-kyr cycle in the $\delta^{13}\text{C}$ is inversely correlated to the filter of the 100-kyr in the MS signal.
274 After 5 m, i.e. after the start of the P-To event, the two filters are in phase. The limestone beds
275 in the Pliensbachian of the atlastic basins originate from exports from the neritic environments,
276 in which the $\delta^{13}\text{C}$ was higher than in pelagic environments (Wilmsen and Neuweiler, 2008). In
277 the Pliensbachian, the $\delta^{13}\text{C}$ is higher in limestone beds. The P-To Event corresponds to a demise
278 in the neritic carbonate production. Fluctuations in the $\delta^{13}\text{C}$ thus correspond to fluctuations in
279 the pelagic production, which is usually higher during the deposit of marlier intervals, when
280 detrital and nutrient increased the primary productivity (Mutterlose and Ruffell, 1999; Mattioli
281 and Pittet, 2004). The demise of the carbonate platforms thus changed the phasing between the
282 MS and the $\delta^{13}\text{C}$, which is a source of uncertainty in the calculation of the durations. Another
283 change of phasing occurs at 28 m, where the $\delta^{13}\text{C}$ and the CaCO_3 content increase. As the
284 phasing between the orbital configuration and the proxies is still unclear, we choose to retain
285 the average duration of 1.00 ± 0.08 myr for the Polymorphum Zone (the uncertainty includes
286 the age model and the duration of a short eccentricity period, see supplementary materials).

287 The spectrum of the calibrated $\delta^{13}\text{C}$ shows a high power at 96 kyr (expected when
288 calibrated to the short eccentricity), 32.4 kyr (main obliquity), 24.1 and 19.7 kyr (precession),
289 and 13.2 to 11.0 kyr (half-precession) (Fig. 7A). In addition, a peak exceeding the 95%
290 confidence level appears at 400 kyr, which corresponds to the long-eccentricity cycle. The
291 spectrum of the calibrated MS shows a high power at 95.7 kyr (expected), 65.5 kyr, 31.9 kyr
292 (main obliquity), from 24.4 to 19.1 kyr (precession), and from 12.1 to 10.6 kyr (half precession)
293 (Fig. 7B). In the $\delta^{13}\text{C}$ and MS signals, the precession cycle has slightly longer periods than
294 expected in the theory (Waltham, 2015). This may be the consequence of a precession cycle
295 missing per short eccentricity. In the astronomical solutions, the amplitude of the precession
296 band is modulated by the 405-kyr and the 100-kyr eccentricity cycles, while the amplitude of
297 the 100-kyr cycle is modulated by the 400-kyr cycle (Laskar et al., 2004). The Taner band-pass

298 filter of the precession cycle in the $\delta^{13}\text{C}$ series was performed with frequency cuts of $3.583 \times$
299 10^{-2} cycles/kyr and 5.417×10^{-2} cycles/kyr, and a roll-off rate of 10^{36} (Fig. 8B, E). We calculated
300 the amplitude modulation (AM) of the precession cycles using a Hilbert transform. The
301 spectrum of the AM of the precession filter shows cycles at 340 kyr (near the 405-kyr
302 eccentricity), and at 123 and 82.8 kyr (near the periods of 124 and 95 kyr of the short
303 eccentricity) (Fig. 8F). We filtered the 100-kyr band of the AM of the precession filter using a
304 Taner band-pass filter with frequency cuts of 6.250×10^{-3} cycles/kyr and 1.558×10^{-2} cycles/kyr
305 and a roll-off rate of 10^{36} (Fig. 8F). The AM of this filter shows a cycle at 340 kyr (Fig. 8G).
306 Similarly, the spectrum of the AM calculated on the direct filter of the 100-kyr band shows a
307 cycle at 436 kyr (Fig. 8H). Thus, the AM of the precession and the 100-kyr eccentricity show
308 similar patterns as expected in the astronomical models. The filters of the two bands shows 11
309 cycles of short eccentricity within the Polymorphum Zone (Fig. 8C), while the various filters
310 of the 405-kyr cycles in the AM of the precession and the 100-kyr cycles show from 3 to 4
311 repetitions of the 405-kyr cycle (Fig. 8A, C, D). The difference between the direct filter and the
312 filter of the AM is explained by the residence time of carbon in the ocean, which creates a delay
313 in the response of the $\delta^{13}\text{C}$ to the orbital forcing (Laurin et al., 2017). In this context of
314 hemipelagic sediments, with the limestone beds originating from exports from neritic
315 environments, the difference may also be due to the change of the carbonate source.

316 The duration of the Polymorphum Zone from this study is longer than the duration of
317 ~ 0.8 myr assessed in the Peniche section (Suan et al., 2008b; Huang and Hesselbo, 2014) and
318 the Foug Tillicht section (Martinez et al., 2017). The correlation of these sections led to a
319 duration of a composite Polymorphum Zone of 0.9-1.0 myr, which agrees with the duration
320 calculated here. In addition, the duration calculated here is in close agreement with the duration
321 estimated from Central Italy, in which 11 bundles of marl-limestone alternations have been
322 related to the 100-kyr eccentricity cycle (Mattioli and Pittet, 2004).

323 The series of condensation affecting the Pliensbachian-Toarcian transition strongly
324 affects the duration assessments in the Northern Tethyan margin. For instance, in the Paris
325 Basin, the duration of the Tenuicostatum Zone (equivalent to Polymorphum) varies from 0.09
326 myr to 0.5 myr (Boulila et al., 2014; Ruebsam et al., 2014). Correlations of $\delta^{13}\text{C}$ curves indicate
327 that these sections are affected by a series of condensation events, leading to an underestimation
328 of the duration of the Tenuicostatum Zone (Pittet et al., 2014). Recently, Boulila and Hinnov
329 (2017) suggested that the 100-kyr eccentricity cycles identified in Suan et al. (2008b) and
330 Huang and Hesselbo (2014) are the record of the obliquity cycle. However, this would imply a
331 hiatus of ~800 kyr in the middle of the Tenuicostatum Zone, which is not indicated in the $\delta^{13}\text{C}$
332 data (Pittet et al., 2014). In addition, detailed observations of the sedimentological pattern of
333 Peniche indicate that these cycles correspond to bundles of 4-6 marl-limestone alternations,
334 which is related to the hierarchy in between the short eccentricity and precession (Suan et al.,
335 2008b). We thus retain here for the Peniche section the astrochronological models from Suan
336 et al. (2008b) and Huang and Hesselbo (2014).

337

338 **5.2 Duration of the P-To Event**

339 The duration of the P-To event varies from ~50 kyr to 0.27 myr from various astrochronological
340 models (Suan et al., 2008b; Huang and Hesselbo, 2014; Martinez et al., 2017). Uncertainties
341 are due to the condensation event often observed at the Pliensbachian-Toarcian boundary (Pittet
342 et al., 2014) and to the difficulty in defining the upper boundary of the P-To event (Martinez et
343 al., 2017). The P-To event indeed starts with an abrupt decrease of 2 to 3‰ the $\delta^{13}\text{C}$ and change
344 in lithology from carbonated to detrital sediment (Suan et al., 2008a; Bodin et al., 2010). Then,
345 the $\delta^{13}\text{C}$ values gently increase, making the definition of an upper limit of the P-To event
346 problematic. Martinez et al. (2017) defined two options to define the upper boundary of the P-
347 To event: (i) the end of the decrease of the $\delta^{13}\text{C}$ and CaCO_3 values; (ii) the local increase of the

348 $\delta^{13}\text{C}$ values in the lower part of the Polymorphum Zone, corresponding to a maximum of the
349 filter of the 405-kyr band in the $\delta^{13}\text{C}$. In the Issouka section, the filter of the 405-kyr band was
350 calculated on the calibrated series (high frequency cut: 0.005833 cycles/kyr; roll-off rate: 10^{36})
351 and converted into depths shows that this maximum is at 13.1 m (Fig. 9). We suggest using this
352 marker as the end of the P-To event, as it can be observed both in the Central High Atlas and
353 the Middle Atlas. From the $\delta^{13}\text{C}$ and the MS age models, the duration of the P-To event as
354 defined here varies from 0.23 to 0.25 myr, with an average duration of 0.24 ± 0.02 myr (this
355 uncertainty takes into account the uncertainty of the age model and the uncertainty of the period
356 of the eccentricity, see supplementary materials). These durations are in agreement with Option
357 1 from the Foug Tillicht section, which vary from 0.25 to 0.29 myr, with an average duration
358 of 0.27 myr (Martinez et al., 2017). This duration of the P-To event appears stable in Moroccan
359 sections, ranging from 0.23 to 0.29 myr.

360

361 **5.3. A synthetic astrochronology for the Tethyan area in the Early Toarcian**

362 The Polymorphum Zone at Issouka shows 10 to 10.5 repetitions of the 100-kyr eccentricity
363 cycles. In comparison, the sedimentary records of Foug Tillicht and Peniche show a total of
364 eight 100-kyr eccentricity cycles for the Polymorphum Zone. Lithological patterns in the
365 Umbria-Marche Basin tend to indicate that the Polymorphum Zone contains ten to eleven
366 repetitions of 100-kyr cycle (Mattioli and Pittet, 2004). Four discontinuities identified in the
367 Pliensbachian-Toarcian transition have affected the completeness of the sedimentary record in
368 the Foug Tillicht and the Peniche sections. In particular, at Peniche, the Pliensbachian-Toarcian
369 transition appears condensed, while in Foug Tillicht the top of Polymorphum is missing
370 (Martinez et al., 2017). In Issouka, Foug Tillicht and Peniche, $\delta^{13}\text{C}$ has been measured at a
371 high resolution and astrochronologies have been produced, making it possible to correlate the
372 sections at a Milankovitch scale.

373 Based on the astrochronological frameworks produced in this study and in Huang and
374 Hesselbo (2014) and Martinez et al. (2017), we can correlate these three sections at the
375 eccentricity scale (Fig. 9). Radiometric ages have been anchored on stratigraphic ages at the
376 Triassic-Jurassic boundary, in the Hettangian and the Sinemurian (Ruhl et al., 2016). A U-Pb
377 age has been proposed for the uppermost part of the Tenuicostatum Zone at 183.22 ± 0.26 Ma
378 in Southern Peru (Sell et al., 2014). The lack of intercalibration with astrochronology makes it
379 difficult to anchor it on our time scale. Conversely, the Triassic-Jurassic boundary have been
380 bracketed at 201.36 ± 0.17 Ma with U-Pb ages from the Pucara Basin (Peru) and the New York
381 Canyon (Nevada, USA), recalibrated applying version 3.0 of EARTHTIME tracer (Wotzlaw et
382 al., 2014). The duration of the interval from the base of the Jurassic to the base of the Toarcian
383 have been assessed at 17.21 myr (Ikeda and Tada, 2014), which matches with the time scale
384 suggested in Ruhl et al. (2016) with an uncertainty of \pm one 405-kyr cycle. It positions the base
385 of the Toarcian at 184.15 ± 0.58 Ma. The uncertainty retained here corresponds to the sum of
386 uncertainties of astrochronology and radiochronology.

387 Other ages are as follows (see also supplementary materials for details of the
388 calculations):

389 - The average duration of the P-To event is 0.24 ± 0.02 myr, positioning the top of the P-To
390 event at 183.91 ± 0.60 myr,

391 - The average duration of the Tenuicostatum/Polymorphum Zone is 1.00 ± 0.08 myr,
392 positioning the top of Tenuicostatum/Polymorphum at 183.15 ± 0.66 Ma. Notice that this age
393 fits with the age of Sell et al. (2014) of 183.22 ± 0.26 Ma for the uppermost part of the
394 Tenuicostatum Zone,

395 - The base of the T-OAE occurs 0.03 myr after the end of the Polymorphum Zone (Huang and
396 Hesselbo, 2014; Fig. 9), i.e. 183.12 ± 0.66 Ma,

397 - The T-OAE encompasses 11 short-eccentricity cycles (Suan et al., 2008b; Huang and
398 Hesselbo, 2014; Thibault et al., 2018), corresponding to a duration of 1.05 ± 0.06 myr (Fig. 9).
399 The top of the T-OAE is thus dated here at 182.07 ± 0.72 Ma,

400

401 **5.4. Origins of P-To and T-OAE disturbances**

402 The large negative CIEs observed in the Early Toarcian, the P-To event and the T-OAE, imply
403 the injection of large amount of light carbon in the oceanic system (Suan et al., 2015). This has
404 been interpreted as dissociation of methane hydrate, maybe orbitally paced (Kemp et al., 2005),
405 or production of thermogenic methane due to volcanic intrusion during the Karoo-Ferrar
406 activity (Svensen et al., 2007). The long duration of the T-OAE (Suan et al., 2008b; Huang and
407 Hesselbo, 2014) implies that the amount of methane needed to maintain the negative excursion
408 for such a long time would exceed the volume of gas hydrate reservoir (Suan et al., 2008b). In
409 addition, the interval of the T-OAE display a positive excursion in Hg/TOC, associated with a
410 volcanic activity (Percival et al., 2015). CA-ID-TIMS U-Pb ages indicate that the Ferrar
411 province activity occurred from 182.779 ± 0.033 Ma and lasted 349 ± 49 kyr (Burgess et al.,
412 2015). These ages fall in the range of the ages assessed here for the T-OAE (183.12 ± 0.66 Ma
413 to 182.07 ± 0.72 Ma; Fig. 9). All these observations tend to favour the crucial role of the Karoo-
414 Ferrar activity on the inception of the T-OAE. Hg/TOC data from Yorkshire and the Peniche
415 sections show a positive excursion within the P-To event, which tend to indicate the
416 concomitance between the P-To event and volcanic activity. The P-To event started $184.15 \pm$
417 0.58 Ma and ended at 183.91 ± 0.60 Ma (Fig. 9), so that the P-To event appears significantly
418 older than the activity of the Ferrar province. Dating of the early phase of the Karoo province
419 tends to indicate that the Karoo province started earlier than the Ferrar (Burgess et al., 2015;
420 Moulin et al., 2017). Notably the oldest $^{40}\text{Ar}/^{39}\text{Ar}$ ages of the Karoo activity have been found
421 in the southern part of the Barkly East Formation (South Africa), within the Omega and the

422 Moshesh's Ford units (Moulin et al., 2017 and references therein). Other ages older than 183
423 Ma have been reported in the Northern part of the Chonke Aike LIP (South America) in the Rio
424 Negro Province and in the eastern part of the Chubut Province (Féraud et al., 1999). The
425 location and the thicknesses of the formations in which these older $^{40}\text{Ar}/^{39}\text{Ar}$ and U/Pb ages
426 have been provided are, to our knowledge, much more limited than that of the main phase of
427 the Karoo-Ferrar activity (~183 Ma). While this main phase is likely to be responsible for the
428 inception of the T-OAE, limited volcanic activities in the early phase of the Karoo and Chonke
429 Aike LIP may have affected the environmental and ecological perturbations recorded at the
430 Pliensbachian-Toarcian boundary.

431

432 **6. Conclusions**

433 The carbon isotope and MS variations in the Late Pliensbachian-Early Toarcian, performed in
434 the expanded hemipelagic in Issouka section from the Middle Atlas Basin, Morocco, reveal
435 superposed frequencies consistent with Milankovitch forcing (eccentricity, obliquity, and
436 precession). The Polymorphum Zone contains 10 to 10.5 repetitions of the 100-kyr eccentricity
437 cycle, so that its duration is assessed here at 1.00 ± 0.08 myr. The duration of the P-To event is
438 in addition assessed at 0.24 ± 0.02 myr. The recognition of the 100-kyr and the 405-kyr
439 eccentricity enabled us to establish a stratigraphic framework between the Northern and the
440 Southern Tethyan margins. Anchoring this framework on published radiometric ages and
441 astrochronological time scales, we could estimate the age of the base of the Toarcian as 184.15
442 ± 0.58 Ma, the top of the P-To event as 183.91 ± 0.60 Ma, the base of the Toarcian OAE as
443 183.12 ± 0.66 Ma, and the top of the Toarcian OAE as 182.07 ± 0.72 Ma. The age of the
444 Toarcian OAE fits with the ages published for the Ferrar volcanic activity. Conversely, the age
445 of the P-To event seems to correspond with early phase of the Karoo and Chonke Aike activity.
446 Thus, the successive and short phases of the volcanic activity of the Chonke Aike, Karoo and

447 Ferrar provinces may have been the smoking gun of the successive phases of the mass
448 extinction observed in marine biotas in the Pliensbachian and Toarcian times.

449

450 **Acknowledgements**

451 This paper benefitted considerably from 3 constructive reviews. We would like to thank also
452 the IAS Postgraduate Grant Scheme for the financial support that Fatima-Zahra Ait-Itto
453 received in 2016 for making the isotopic analyses at Plymouth University. Mathieu Martinez
454 was supported by ERC Consolidator Grant Earthsequencing.

455

456 **References**

457 Ait Addi, A., Chafiki, D., 2013. Sedimentary evolution and palaeogeography of mid Jurassic
458 deposits of the Central High Atlas, Morocco. *J. Afr. Earth Sci.* 84, 54–69.
459 <https://doi.org/10.1016/j.jafrearsci.2013.04.002>.

460 Ait-Itto, F.-Z., Price, G.D., Ait Addi, A., Chafiki, D., Mannani, I., 2017. Bulk-carbonate and
461 belemnite carbon-isotope records across the Pliensbachian-Toarcian boundary on the
462 northern margin of Gondwana (Issouka, Middle Atlas, Morocco). *Palaeogeogr.*
463 *Palaeoclim. Palaeoecol.* 466, 128–136. <https://doi.org/10.1016/j.palaeo.2016.11.014>.

464 Bassoulet, J.P., Baudin, F., 1994. Le Toarcien inférieur : une période de crise dans les bassins
465 et sur les plate-formes carbonatées de l'Europe du Nord-Ouest et de la Téthys. *Geobios.*
466 17, 645–654. [https://doi.org/10.1016/S0016-6995\(94\)80227-0](https://doi.org/10.1016/S0016-6995(94)80227-0).

467 Bassoulet, J., Elmi, S., Poisson, F., Cecca, F., Belion, Y., Guiraud, R., Baudin, F., 1993. Mid
468 Toarcian. In: Dercourt, J., Ricou, L.E., Vrielynck, B. (Eds.), *Atlas Tethys,*
469 *Paleoenvironmental Maps: Becip–Franlab, Rueil–Malmaison, France,* 63–80.

470 Bejjaji, Z., Chakiri, S., Reolid, M., Boutakiout, M., 2010. Foraminiferal biostratigraphy of the
471 Toarcian deposits (Lower Jurassic) from the Middle Atlas (Morocco). Comparison with

472 western Tethyan areas. *J. Afr. Earth Sci.* 57, 154–162.
473 <https://doi.org/10.1016/j.jafrearsci.2009.08.002>.

474 Berger, A., Loutre, M.F., Melice, J.L., 2006. Equatorial insolation: from precession harmonics
475 to eccentricity frequencies. *Clim. Past* 2, 131–136. [https://doi.org/10.5194/cp-2-131-](https://doi.org/10.5194/cp-2-131-2006)
476 2006.

477 Bodin, S., Mattioli, E., Fröhlich, S., Marshall, J.D., Boutib, L., Lahsini, S., Redfern, J., 2010.
478 Toarcian carbon isotope shifts and nutrient changes from the Northern margin of
479 Gondwana (High Atlas, Morocco, Jurassic): Palaeoenvironmental implications.
480 *Palaeogeogr. Palaeoclimatol.* 297, 377–390. <https://doi.org/10.1016/j.palaeo.2010.08.018>.

481 Boulila, S., Galbrun, B., Huret, E., Hinnov, L.A., Rouget, I., Gardin, S., Bartolini, A., 2014.
482 Astronomical calibration of the Toarcian Stage: Implications for sequence stratigraphy
483 and duration of the early Toarcian OAE. *Earth and Planet. Sci. Lett.* 386, 98–111.
484 <https://doi.org/10.1016/j.epsl.2013.10.047>.

485 Boulila, S., Hinnov L.A., 2017. A review of tempo and scale of the early Jurassic Toarcian
486 OAE: implications for carbon cycle and sea level variations. *Newsl. Stratigr.* In press.
487 <https://doi.org/10.1127/nos/2017/0374>.

488 Burgess, S.D., Bowring, S.A., Fleming, T.H., Elliot, D.H., 2015. High-precision geochronology
489 links the Ferrar large igneous province with early-Jurassic ocean anoxia and biotic crisis.
490 *Earth Planet. Sci. Lett.* 415, 90–99. <https://doi.org/10.1016/j.epsl.2015.01.037>.

491 Cleveland, W.S., 1979. Robust Locally Weighted Regression and Smoothing Scatterplots.
492 *Journal of the American Statistical Association* 74, 829-836.

493 Dera, G., Brigaud, B., Monna, F., Laffont R., Pucéat, E., Deconinck, J.-F., Pellenard, P.,
494 Joachimski, M.M., Durlet, C., 2011. Climatic ups and downs in a disturbed Jurassic
495 world. *Geology* 39, 215–218. <http://dx.doi.org/10.1130/G31579.1>.

496 Du Dresnay, R., 1971. Extension et développement des phénomènes récifaux Jurassique dans
497 le domaine Atlasique Marocain, particulièrement au Lias moyen. *Bull. Soc. Geol. Fr.*
498 13, 46–56. <http://dx.doi.org/10.2113/gssgfbull.S7-XIII.1-2.46>.

499 El Hammichi, F., Benschili, K., Elmi, S., 2008. Les faunes d'Ammonites du Toarcien-Aalénien
500 du Moyen Atlas sud-occidental (Maroc). *Rev. Paléobiol.* 27, 429–447.

501 Féraud, G., Alric, V., Fornari, M., Bertrand, H., Haller, M., 1999. $^{40}\text{Ar}/^{39}\text{Ar}$ dating of the
502 Jurassic volcanic province of Patagonia: migrating magmatism related to Gondwana
503 break-up and subduction. *Earth Planet. Sci. Lett.* 172, 83–96.
504 [https://doi.org/10.1016/S0012-821X\(99\)00190-9](https://doi.org/10.1016/S0012-821X(99)00190-9).

505 Hallam, A., 1997. Estimates of the amount and rate of the of sea level change across the
506 Rhaetian–Hettangian and Pliensbachian–Toarcian boundary (latest Triassic to Early
507 Jurassic). *J. Geol. Soc. Lond.* 154, 773–779.
508 <http://dx.doi.org/10.1144/gsjgs.154.5.0773>.

509 Hesselbo, S.P., Jenkyns, H.C., Duarte, L.V., Oliveira, L.C.V., 2007. Carbon–isotope record of
510 the Early Jurassic (Toarcian) Oceanic Anoxic Event from fossil wood and marine
511 carbonate (Lusitanian Basin, Portugal). *Earth Planet. Sci. Lett.* 253, 455–470.
512 <https://doi.org/10.1016/j.epsl.2006.11.009>.

513 Huang, C., Hesselbo, S.P., 2014. Pacing of the Toarcian Oceanic Anoxic Event (Early Jurassic)
514 from astronomical correlation of marine sections. *Gondwana Res.* 25, 1348–1356.
515 <https://doi.org/10.1016/j.gr.2013.06.023>.

516 Ikeda, M., Tada, R., 2014. A 70 million year astronomical time scale for the deep-sea bedded
517 chert sequence (Inuyama, Japan): Implications for Triassic–Jurassic geochronology.
518 *Earth Planet. Sci. Lett.* 399, 30–43. <https://doi.org/10.1016/j.epsl.2014.04.031>.

519 Jenkyns, H.C., 1988. The Early Toarcian anoxic event: stratigraphic, sedimentary and
520 geochemical evidence. *Am. J. Sci.* 288, 101–151.

521 Kemp, D.B., Coe, A.L., Cohen, A.S., Schwark, L., 2005. Astronomical pacing of methane
522 release in the Early Jurassic period. *Nature* 437, 396–399.
523 <http://dx.doi.org/10.1038/nature04037>.

524 Lachkar, N., Guiraud, M., El Harfi, A., Dommergues, J. L., Dera, G., Durllet, C., 2009. Early
525 Jurassic normal faulting in a carbonate extensional basin: characterization of
526 tectonically driven platform drowning (High Atlas rift, Morocco). *J. Geol. Soc. Lond.*
527 166, 413–430. <http://dx.doi.org/10.1144/0016-76492008-084>.

528 Lamas, F., Irigaray, C., Oteo, C., Chacón, J., 2005. Selection of the most appropriate method
529 to determine the carbonate content for engineering purposes with particular regard to
530 marls. *Eng. Geol.* 81, 32–41. <https://doi.org/10.1016/j.enggeo.2005.07.005>.

531 Laskar, J., Robutel, P., Joutel, F., Gastineau, M., Correia, A.C.M., Levrard, M., 2004. A long-
532 term numerical solution for the insolation quantities of the Earth. *Astronom. Astrophys.*
533 428, 261–285. <https://doi.org/10.1051/0004-6361:20041335>.

534 Laurin, J., Růžek, B., Giorgioni, M., 2017. Orbital Signals in Carbon Isotopes: Phase Distortion
535 as a Signature of the Carbon Cycle. *Paleoceanography* 32, 1236–1255.
536 <http://dx.doi.org/10.1002/2017PA003143>.

537 Little, C.T.S., Benton, M.J., 1995. Early Jurassic mass extinction: a global long-term event.
538 *Geology* 23, 495–498.
539 [http://dx.doi.org/10.1130/0091-7613\(1995\)023<0495:EJMEAG>2.3.CO;2](http://dx.doi.org/10.1130/0091-7613(1995)023<0495:EJMEAG>2.3.CO;2).

540 Littler, K., Hesselbo, S.P., Jenkyns, H.C., 2010. A carbon-isotope perturbation at the
541 Pliensbachian–Toarcian boundary: evidence from the Lias Group, NE England.
542 *Geological Magazine* 147, 181–192. <https://doi.org/10.1017/S0016756809990458>.

543 Kemp, D.B., 2016. Optimizing significance testing of astronomical forcing in
544 cyclostratigraphy. *Paleoceanography* 31, <https://doi.org/10.1002/2016PA002963>.

545 Mann, M.E., Lees, J.M., 1996. Robust estimation of background noise and signal detection in
546 climatic time series. *Climatic Change* 33, 409–445.
547 <http://dx.doi.org/10.1007/BF00142586>.

548 Martinez, M., Deconinck, J.-F., Pellenard, P., Riquier, L., Company, M., Reboulet, S., Moiroud,
549 M., 2015. Astrochronology of the Valanginian-Hauterivian stages (Early Cretaceous):
550 chronological relationships between the Paraná–Etendeka large igneous province, the
551 Weissert and the Faraoni events. *Global Planet. Change* 131, 158–173.
552 <https://doi.org/10.1016/j.gloplacha.2015.06.001>.

553 Martinez, M., Kotov, S., De Vleeschouwer, D., Pas, D., Pälike, H., 2016. Testing the impact of
554 stratigraphic uncertainty on spectral analyses of sedimentary series. *Clim. Past* 12,
555 1765–1783. <https://doi.org/10.5194/cp-12-1765-2016>.

556 Martinez, M., Krencker, F.N., Mattioli E., Bodin, S., 2017. Orbital chronology of the
557 Pliensbachian–Toarcian transition from the Central High Atlas Basin (Morocco).
558 *Newsletters on Stratigraphy* 50, 47–69. <https://doi.org/10.1127/nos/2016/0311>.

559 Mattioli, E., Pittet, B., 2004. Spatial and temporal distribution of calcareous nannofossils along
560 a proximal–distal transect in the Lower Jurassic of the Umbria–Marche Basin (central
561 Italy). *Palaeogeogr. Palaeoclim. Palaeoecol.* 205, 295–316.
562 <https://doi.org/10.1016/j.palaeo.2003.12.013>.

563 Meyers, S.R., Sageman, B.B., 2007. Quantification of deep-time orbital forcing by average
564 spectral misfit. *Am. J. Sci.* 307, 773–792. <http://dx.doi.org/10.2475/05.2007.01>.

565 Meyers, S.R., 2012. Seeing red in cyclic stratigraphy: Spectral noise estimation for
566 astrochronology. *Paleoceanography* 27, PA 3228.
567 <http://dx.doi.org/10.1029/2012PA002307>.

568 Meyers, S.R., 2014. Astrochron: An R Package for Astrochronology. [Available at [http://cran.r-](http://cran.r-project.org/package=astrochron)
569 [project.org/package=astrochron](http://cran.r-project.org/package=astrochron).]

570 Michard, A., 1976. *Eléments de géologie Marocaine. Notes et Mémoires du Service Géologique*
571 252, 408.

572 Moulin, M., Fluteau, F., Courtillot, V., Marsh, J., Delpech, G., Quidelleur, X., and Gérard, M.,
573 2017. Eruptive history of the Karoo lava flows and their impact on early Jurassic
574 environmental change. *J. Geophys. Res. Solid Earth.* 122, 738–772.
575 <http://dx.doi.org/10.1029/2011JB008210>.

576 Mutterlose, J., Ruffell, A., 1999. Milankovitch-scale palaeoclimate changes in pale-dark
577 bedding rhythms from the Early Cretaceous (Hauterivian and Barremian) of eastern
578 England and northern Germany. *Palaeogeogr. Palaeoclim. Palaeoecol.* 154, 133–160.
579 [https://doi.org/10.1016/S0031-0182\(99\)00107-8](https://doi.org/10.1016/S0031-0182(99)00107-8).

580 Percival, L.M.E., Witt, M.L.I., Mather, T.A., Hermoso, M., Jenkyns, H.C., Hesselbo, S.P., Al-
581 Suwaidi, A.H., Storm, M.S., Xu, W., Ruhl, M., 2015. Globally enhanced mercury
582 deposition during the end-Pliensbachian extinction and Toarcian OAE: a link to the
583 Karoo–Ferrar Large Igneous Province. *Earth Planet. Sci. Lett.* 428, 267–280.
584 <https://doi.org/10.1016/j.epsl.2015.06.064>.

585 Pittet, B., Suan, G., Lenoir, F., Duarte, L.V., Mattioli E., 2014. Carbon isotope evidence for
586 sedimentary discontinuities in the lower Toarcian of the Lusitanian Basin (Portugal):
587 Sea level change at the onset of the Oceanic Anoxic Event. *Sediment. Geol.* 303, 1–14.
588 <https://doi.org/10.1016/j.sedgeo.2014.01.001>.

589 Ruebsam, W., Münzberger, P. and Schwark, L., 2014. Chronology of the Early Toarcian
590 environmental crisis in the Lorraine Sub-Basin (NE Paris Basin). *Earth Planet. Sci. Lett.*
591 404, 273–282. <https://doi.org/10.1016/j.epsl.2014.08.005>.

592 Ruhl, M., Hesselbo, S.P., Hinnov, L., Jenkyns, H.C., Xu, W., Riding, J.B., Storm, M., Minisini,
593 D., Ullmann, C.V., Leng, M.J., 2016. Astronomical constraints on the duration of the

594 Early Jurassic Pliensbachian Stage and global climatic fluctuations. *Earth Planet. Sci.*
595 *Lett.* 455, 149–165. <https://doi.org/10.1016/j.epsl.2016.08.038>.

596 Sell, B., Ovtcharova, M., Guex, J., Bartolini, A., Jourdan, F., Spangenberg, J.E., Vicente, J.,
597 Schaltegger, U., 2014. Evaluating the temporal link between the Karoo LIP and
598 climatic–biologic events of the Toarcian Stage with high-precision U–Pb
599 geochronology. *Earth Planet. Sci. Lett.* 408, 48–56.
600 <https://doi.org/10.1016/j.epsl.2014.10.008>.

601 Studer, M., Du Dresnay, R., 1980. Déformations synsédimentaires en compression pendant le
602 Lias supérieur et le Dogger, au Tizi n'Irhil (Haut Atlas central de Midelt, Maroc). *Bull.*
603 *Soc. Geol. Fr.* 22, 391–397. <http://dx.doi.org/10.2113/gssgfbull.S7-XXII.3.391>.

604 Suan, G., Mattioli, E., Pittet, B., Mailliot, S. and Lécuyer, C., 2008a. Evidence for major
605 environmental perturbation prior to and during the Toarcian (Early Jurassic) oceanic
606 anoxic event from the Lusitanian Basin, Portugal. *Paleoceanography.* 23, PA1202.
607 <http://dx.doi.org/10.1029/2007PA001459>.

608 Suan, G., Pittet, B., Bour, I., Mattioli, E., Duarte, L. and Mailliot, S., 2008b. Duration of the
609 Early Toarcian carbon isotope excursion deduced from spectral analysis: Consequence
610 for its possible causes. *Earth Planet. Sci. Lett.* 267, 666–679.
611 <https://doi.org/10.1016/j.epsl.2007.12.017>.

612 Suan, G., van de Schootbrugge, B., Adatte, T., Fiebig, J., Oschmann, W., 2015. Calibrating the
613 magnitude of the Toarcian carbon cycle perturbation. *Paleoceanography.* 30,
614 PA002758. <http://dx.doi.org/10.1002/2014PA002758>.

615 Svensen, H., Planke, S., Chevallier, L., Malthe-Sorensen, A., Corfu, F., Jamtveit, B., 2007.
616 Hydrothermal venting of greenhouse gases triggering Early Jurassic global warming.
617 *Earth Planet. Sci. Lett.* 256, 554–566. <https://doi.org/10.1016/j.epsl.2007.02.013>.

618 Taner, M.T., 2003. Attributes Revisited, Technical Publication. Rock Solid Images, Inc.,
619 Houston, TX (URL: rocksolidimages.com/pdf/attrib_revisited.htm).

620 Thibault, N., Rhul, M., Ullmann, C.V., Korte, C., Kemp, D.B., Gröcke, D.R., Hesselbo, S.P.,
621 2018. The wider context of the Lower Jurassic Toarcian oceanic anoxic event in
622 Yorkshire coastal outcrops, UK. Proceedings of the Geologists' Association, in press.
623 <https://doi.org/10.1016/j.pgeola.2017.10.007>.

624 Vaughan, S., Bailey, R.J., Smith, D.G., 2015. Cyclostratigraphy: data filtering as a source of
625 spurious spectral peaks. Geological Society, London, Special Publications 404, 151-
626 156. <https://doi.org/10.1144/SP404.11>.

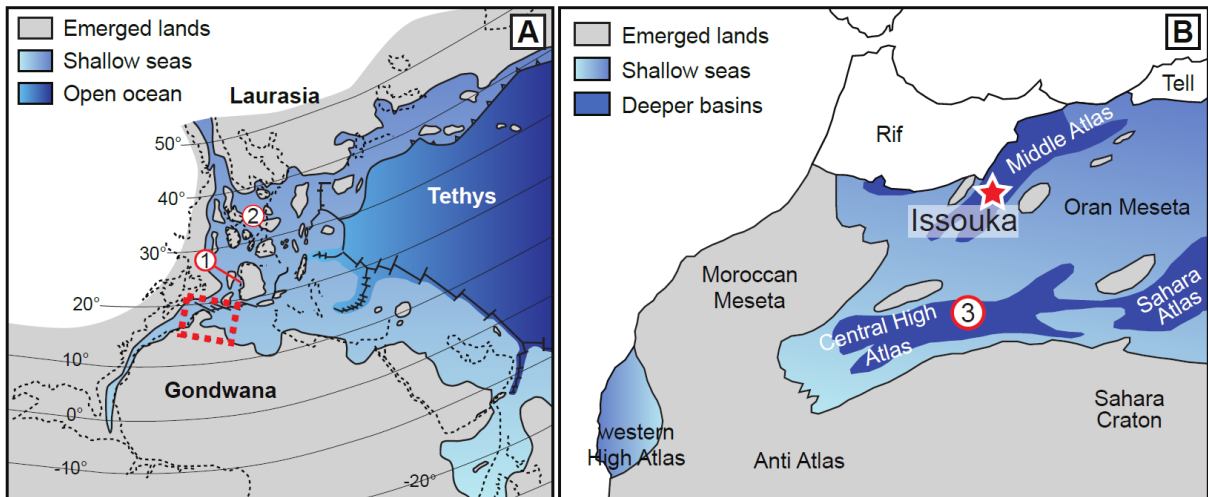
627 Weedon, G.P., 2003. Time-Series Analysis and Cyclostratigraphy: Examining stratigraphic
628 records of environmental cycles. Cambridge University Press, Cambridge.

629 Waltham, D., 2015. Milankovitch Period Uncertainties and Their Impact on Cyclostratigraphy.
630 J. Sediment. Res. 85, 990–998. <http://dx.doi.org/10.2110/jsr.2015.66>.

631 Wilmsen, M. and Neuweiler, F., 2008. Biosedimentology of the Early Jurassic post-extinction
632 carbonate depositional system, central High Atlas rift basin, Morocco. Sedimentology
633 55, 773–807. <http://dx.doi.org/10.1111/j.1365-3091.2007.00921.x>.

634 Wotzlaw, J.-F., Guex, J., Bartolini, A., Gallet, Y., Krystyn, L., McRoberts, C.A., Taylor, D.,
635 Schoene, B., Schaltegger, U., 2014. Towards accurate numerical calibration of the Late
636 Triassic: high-precision U–Pb geochronology constraints on the duration of the
637 Rhaetian. Geology. 42, 571–574. <http://dx.doi.org/10.1130/G35612.1>.

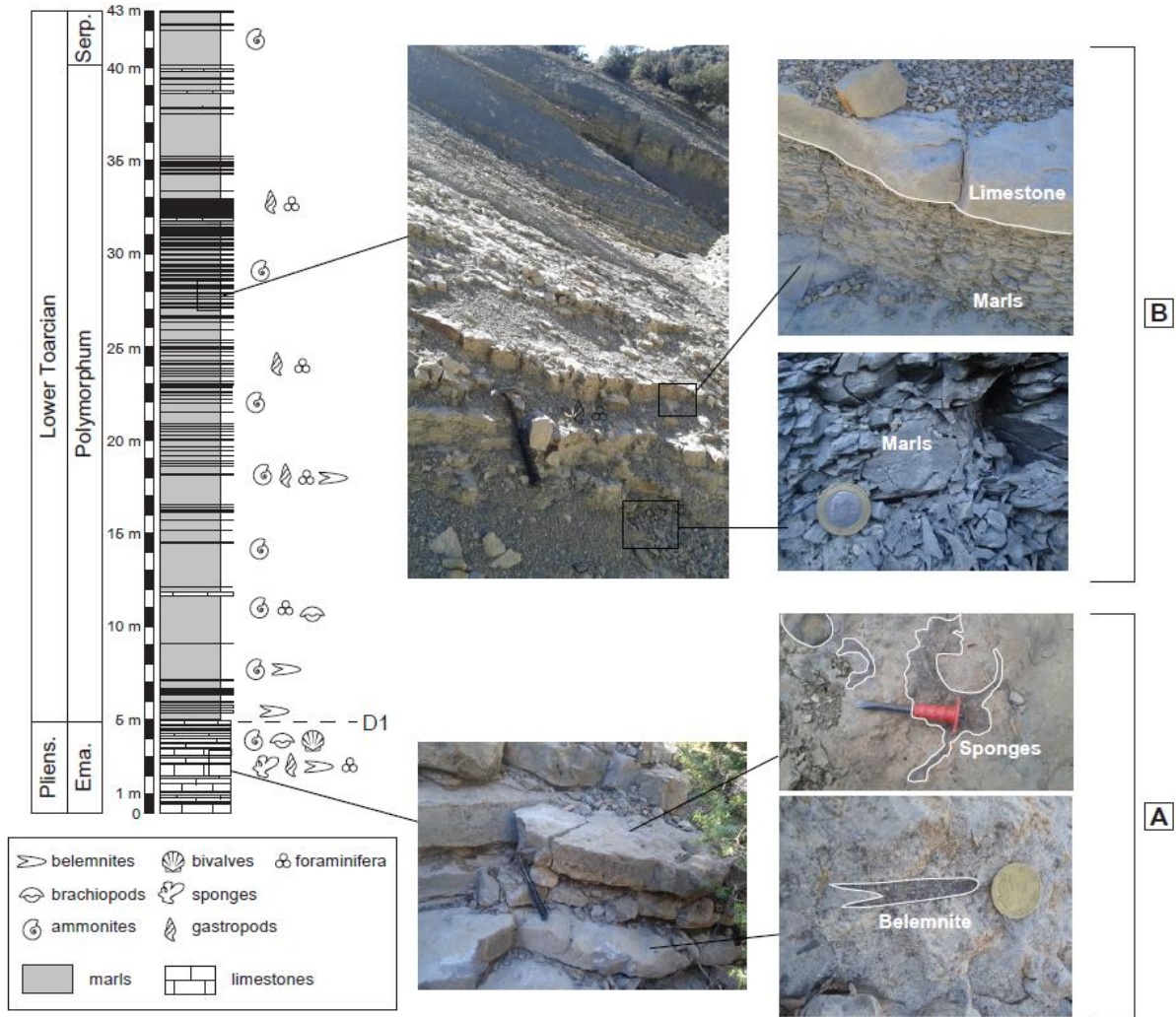
638



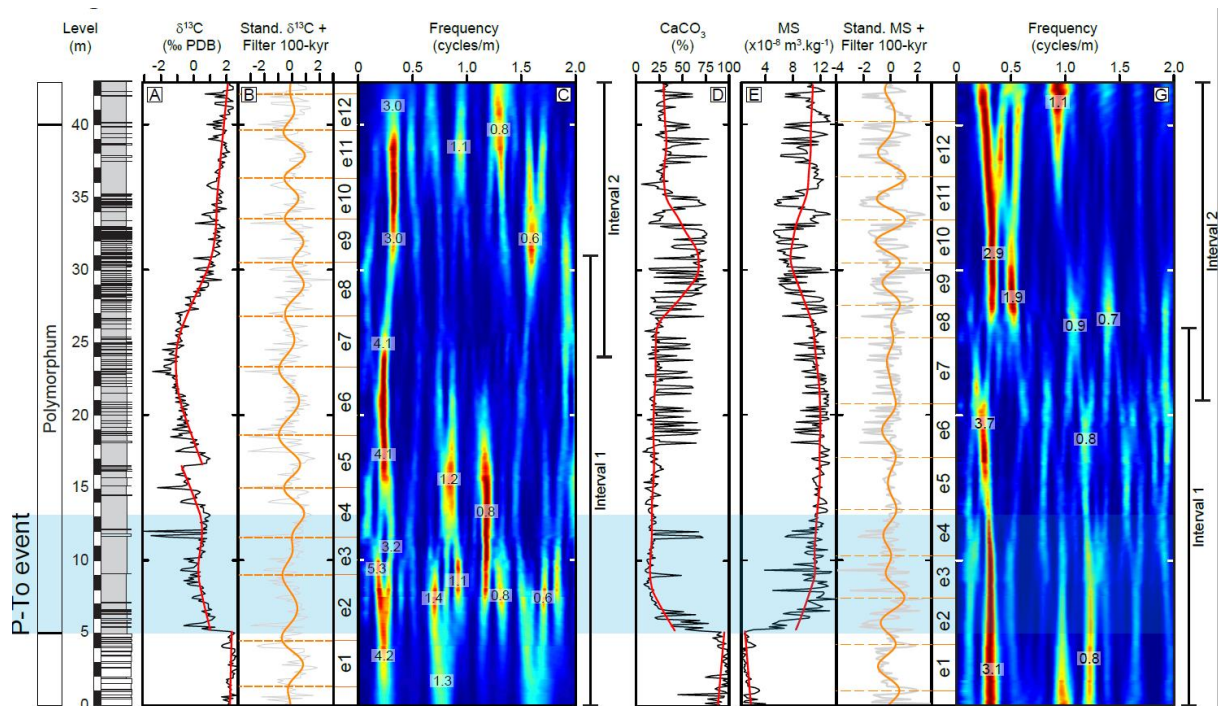
639

640

641 Fig. 1. Geological setting of the Issouka section. **A.** Palaeogeographic map of the western Tethys during
 642 the Early Jurassic. The red dash rectangle shows the limit of the second map. Label “1” indicates the
 643 location of the Peniche section. Label “2” indicates the location of Yorkshire area. **B.** Geographical map
 644 of Morocco and western Algeria showing the main geological provinces and the location of the Issouka
 645 section within the Middle Atlas. Label “3” indicates the location of the Fom Tillicht section (maps
 646 from Bodin et al., 2010).

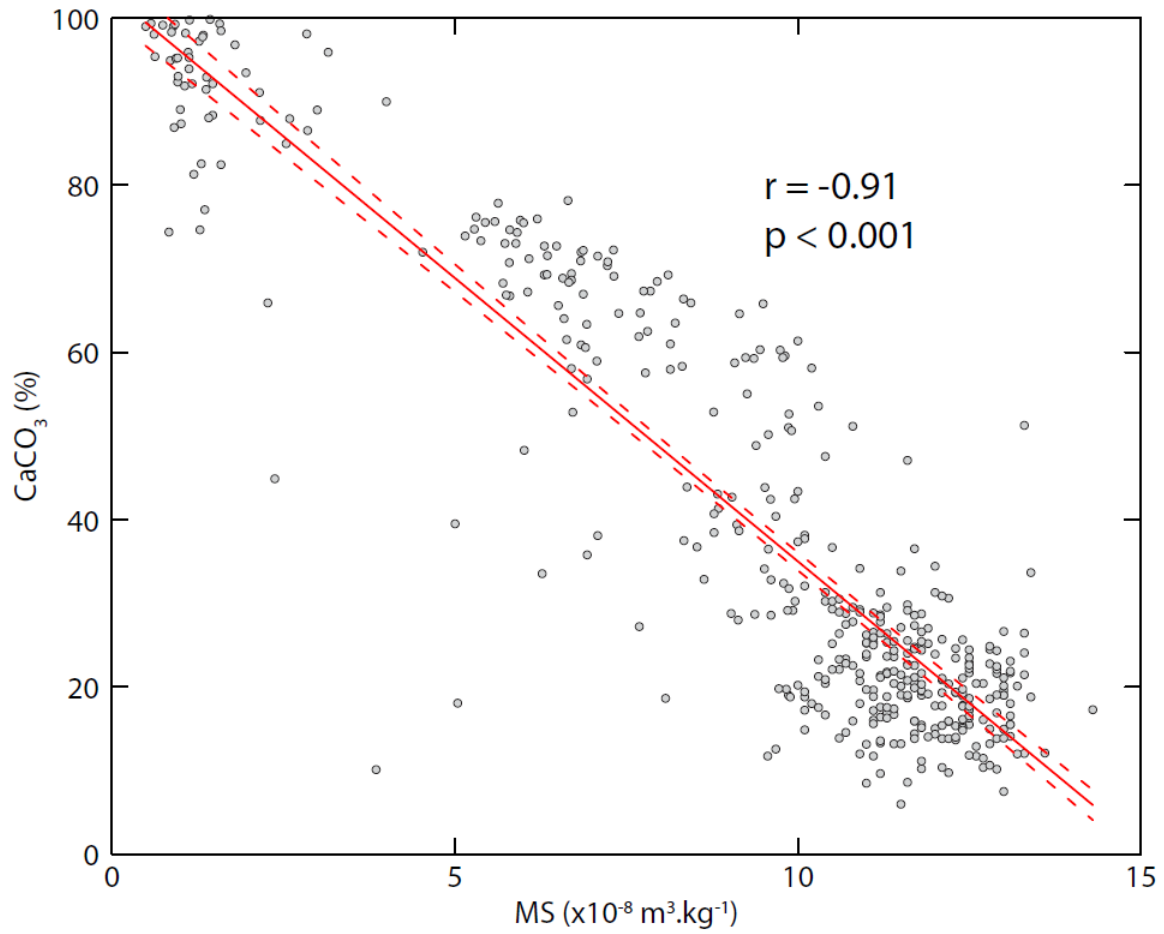


648 Fig. 2. The different facies in the Issouka section. **A.** Limestone of the late Pliensbachian with
 649 fauna (belemnites, sponges and brachiopods). **B.** The Lower Toarcian, characterized by grey
 650 marls and limestone intercalations.



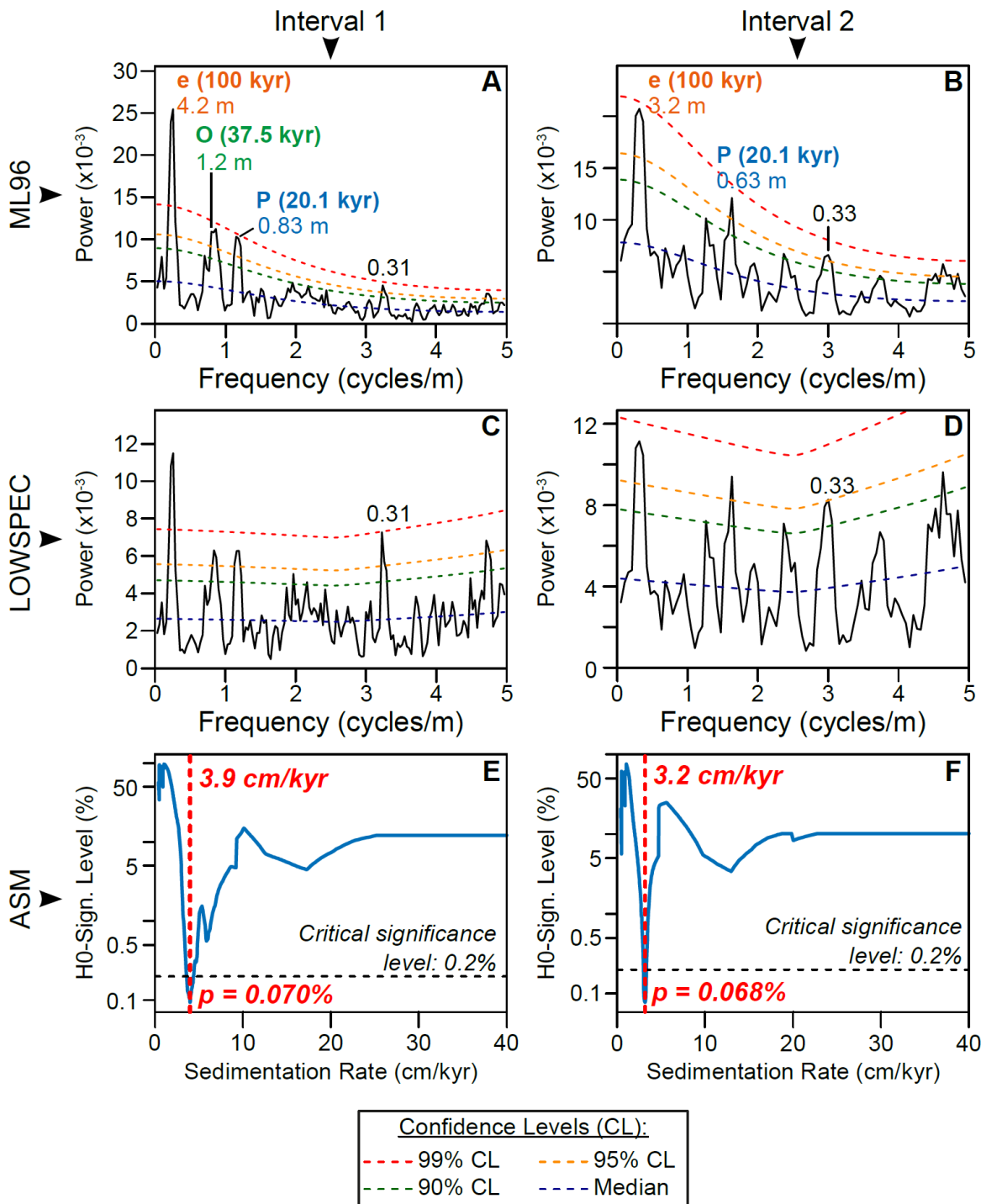
651

652 Fig. 3. Raw data, spectrograms and filters of the 100-kyr eccentricity band of the carbon isotope ($\delta^{13}\text{C}$)
 653 and magnetic susceptibility (MS) signals. **A.** Raw $\delta^{13}\text{C}$ signal (in black) with long-term trend (in red).
 654 **B.** Standardised $\delta^{13}\text{C}$ signal (in grey) with the filter of the 100-kyr eccentricity (in orange). **C.**
 655 Spectrogram of the $\delta^{13}\text{C}$ signal performed with 15-m-width windows. **D.** Raw CaCO_3 signal (in black)
 656 with long-term trend (in red). **E.** Raw MS signal (in black) with long-term trend (in red). **F.** Standardised
 657 MS signal (in grey) with the filter of the 100-kyr eccentricity (in orange). **G.** Spectrogram of the MS
 658 signal performed with 15-m-width windows.



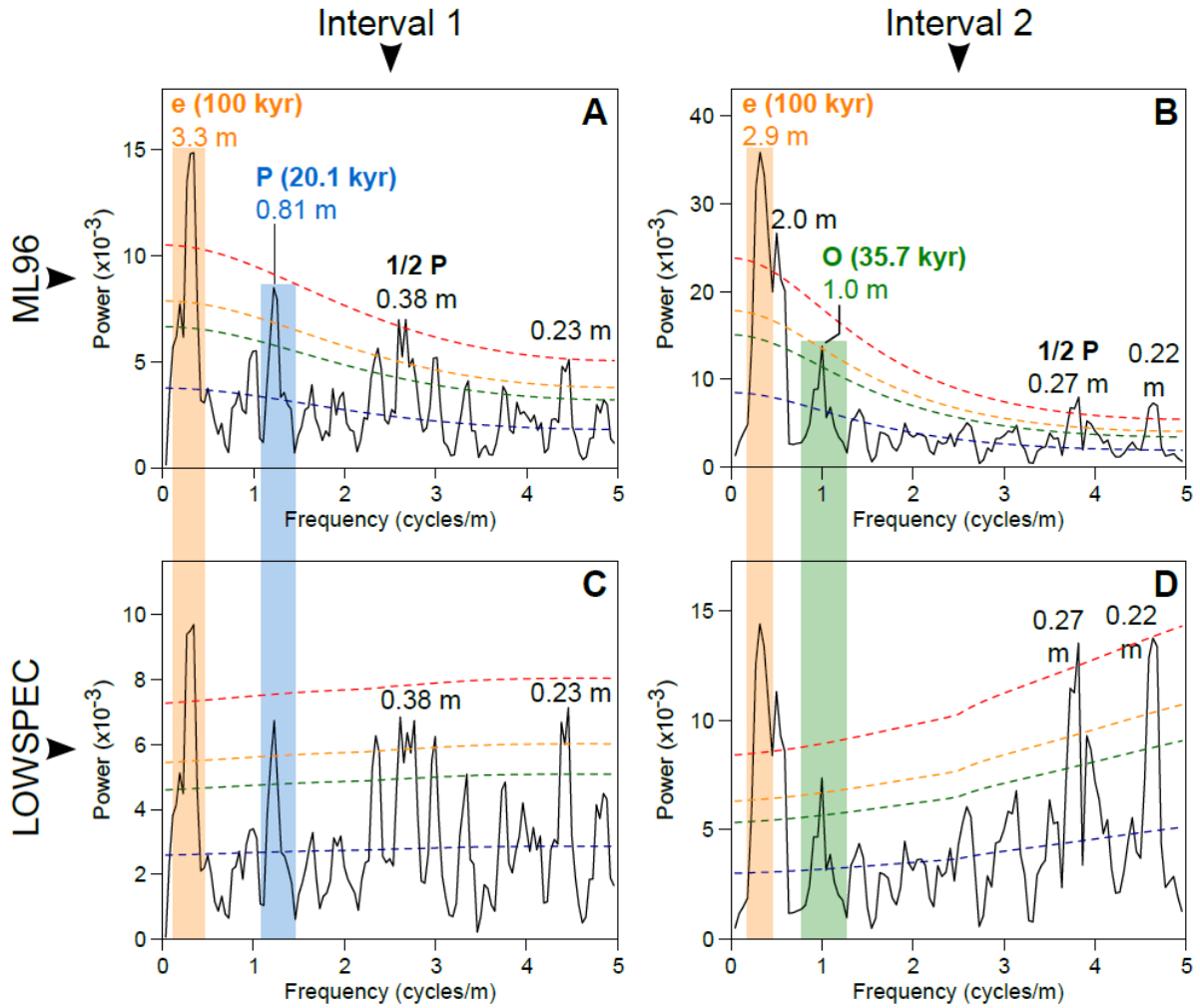
659

660 Fig. 4. Cross-plot of the magnetic susceptibility (MS) versus calcium carbonate content
661 (CaCO₃). The full red line is the best-fit linear regression, while dash lines are the 95%
662 confidence intervals of the linear regression. r indicates the coefficient correlation, and p is the
663 p -value of the correlation.



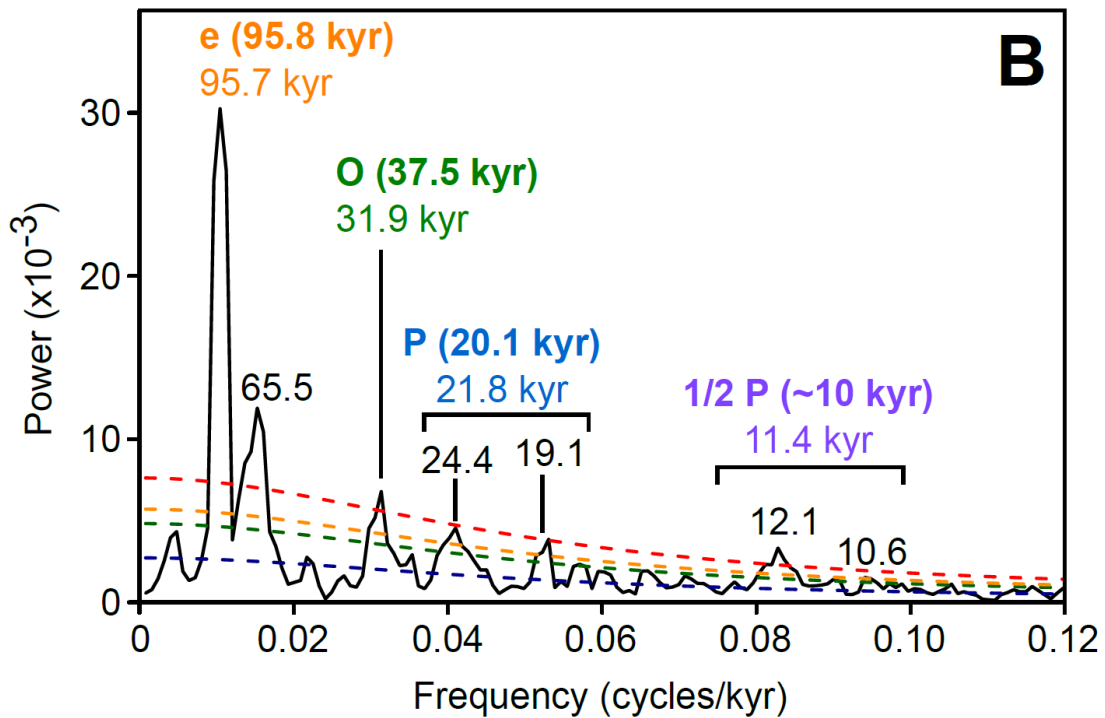
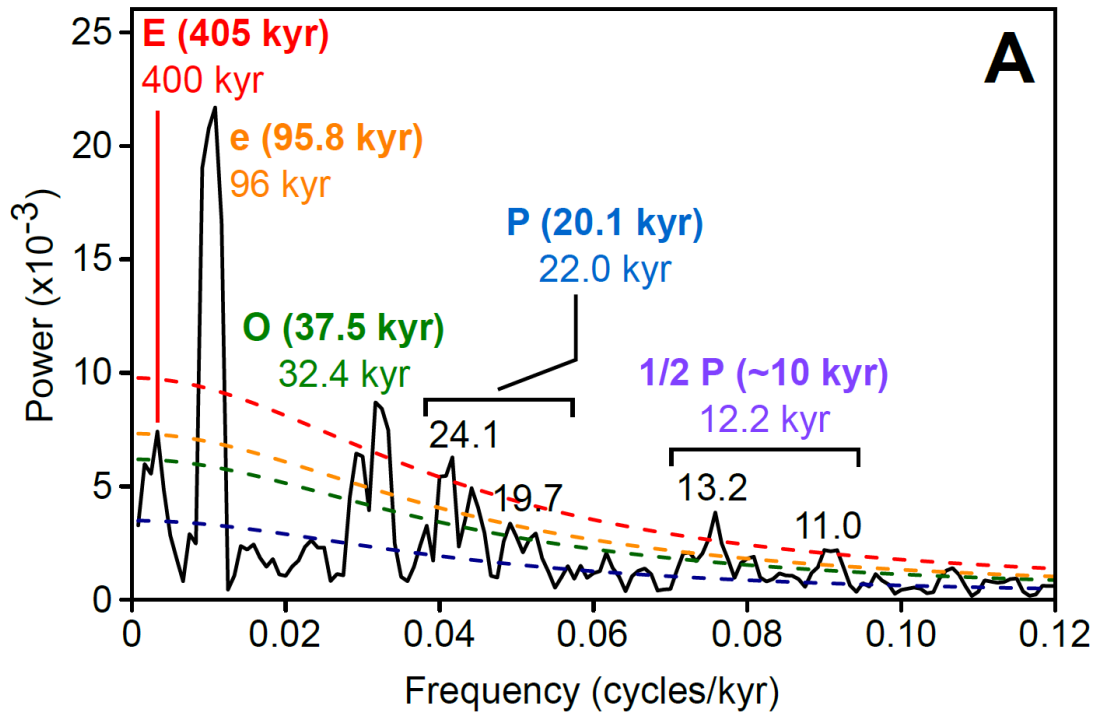
664

665 Fig. 5. 2π -MTM spectra and ASM results of the $\delta^{13}\text{C}$ series. **A. and B.** Spectra of intervals 1
 666 and 2 with confidence levels calculated with the Mann and Lees (1996) method (ML96) with a
 667 Tukey's endpoint rule (Meyers, 2014). **C. and D.** Spectra of intervals 1 and 2 with confidence
 668 levels calculated with the LOWSPEC method (Meyers, 2012). **E. and F.** H0 significance levels
 669 from the ASM applied on intervals 1 and 2. The red dashed line indicates the sedimentation
 670 rate for which the sedimentary frequencies fit the best with the orbital frequencies.



671

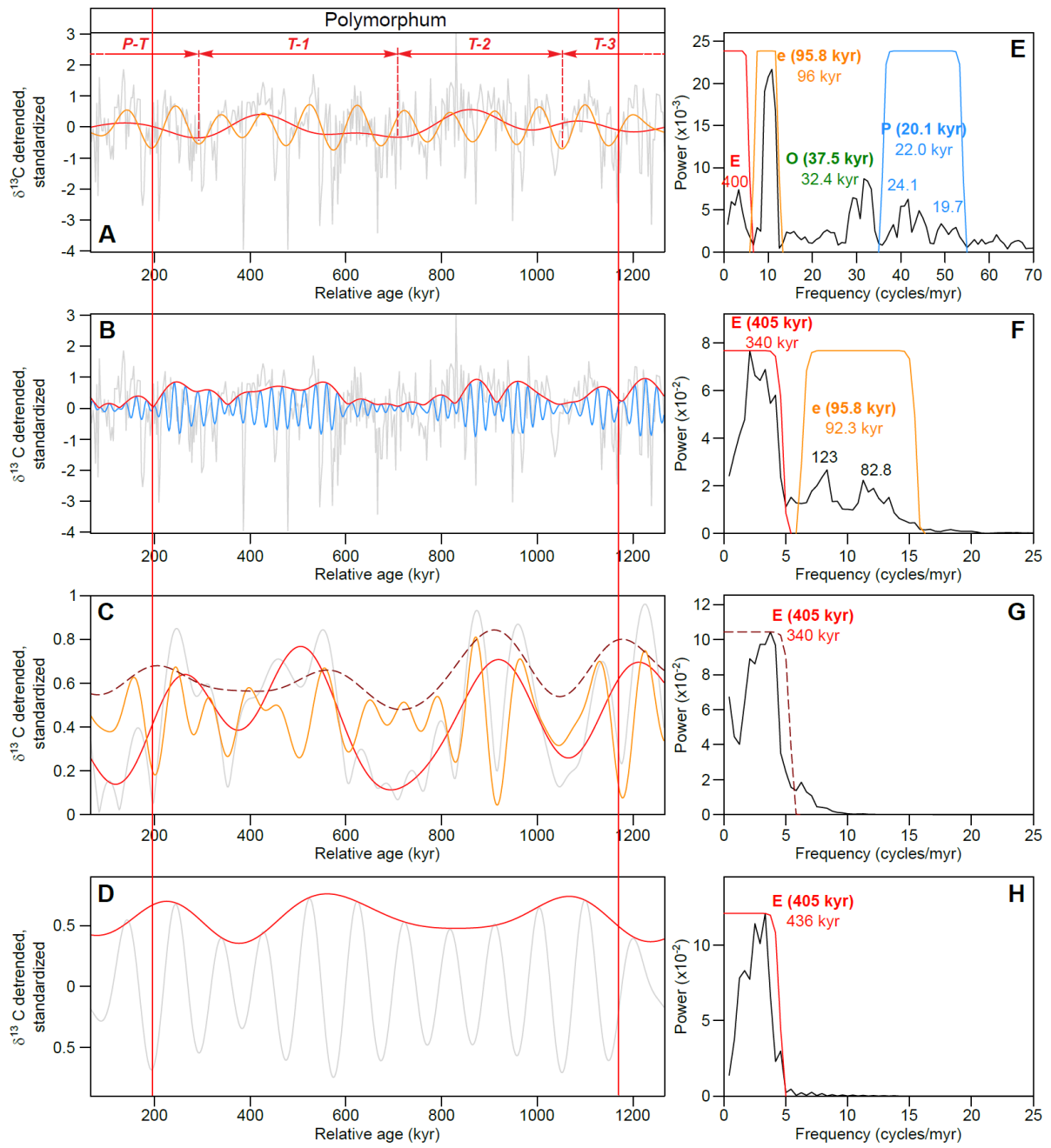
672 Fig. 6. 2π -MTM spectra of the magnetic susceptibility. **A. and B.** Spectra of intervals 1 and 2
 673 with confidence levels calculated with the Mann and Lees (1996) method (ML96) with a
 674 Tukey's endpoint rule (Meyers, 2014). **C. and D.** Spectra of intervals 1 and 2 with confidence
 675 levels calculated with the LOWSPEC method (Meyers, 2012).



676

677 Fig. 7. 2π -MTM spectra of the (A.) calibrated $\delta^{13}\text{C}$ series, and (B.) calibrated MS series. The
 678 main periods are labeled in kyr. The theoretical period of the corresponding astronomical cycle
 679 is displayed in brackets. Abbreviations: E: 400-kyr eccentricity; e: 100-kyr eccentricity; O:
 680 obliquity.

681



682

683 Fig. 8.

684

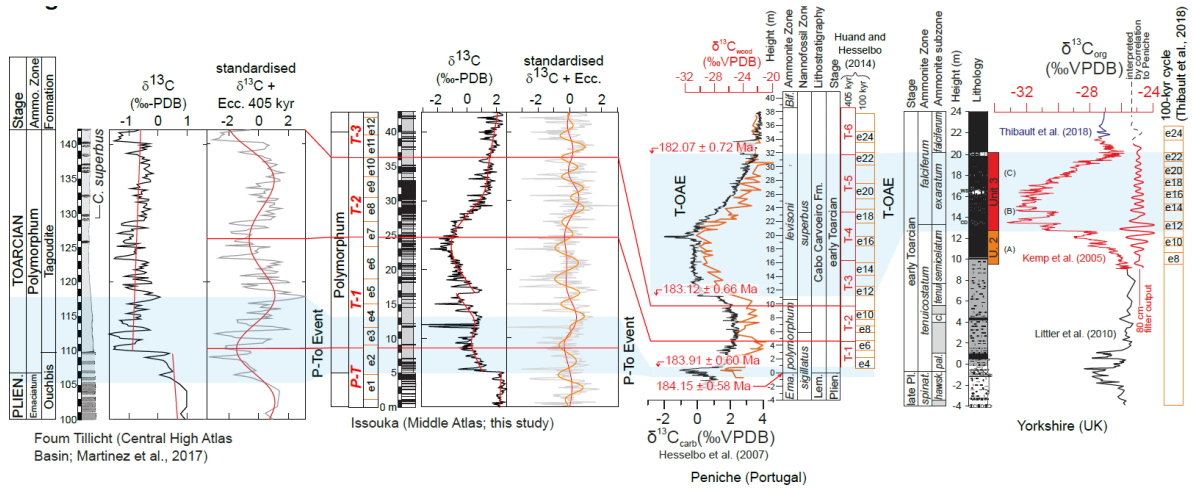
685

686

687

688

689 Fig. 8. Comparison between the direct filters of the eccentricity on the calibrated $\delta^{13}\text{C}$ signal
690 and the amplitude modulation of the precession in the calibrated $\delta^{13}\text{C}$. **A.** Filter of the 405-kyr
691 eccentricity (in red) and the 100-kyr eccentricity (in orange) of the calibrated $\delta^{13}\text{C}$ signal (in
692 grey). **B.** Filter of the precession (in blue) and its amplitude modulation (in red) of the calibrate
693 $\delta^{13}\text{C}$ signal (in grey). **C.** Filter of the 100-kyr cycle (in orange) and the 405-kyr cycle (in red)
694 obtained from the amplitude modulation of the precession cycle (in grey). In dashed brown:
695 Filter of the 405-kyr cycle obtained from the 100-kyr band of the amplitude modulation of the
696 precession. **D.** Filter of the 405-kyr cycle obtained from the amplitude modulation of the direct
697 filter of the 100-kyr cycle (in grey). **E.** Spectrum of the calibrated $\delta^{13}\text{C}$ series, with the filters
698 used for the 405-kyr cycle (in red; frequency cut: 0.005833 cycles/kyr; roll-off rate: 10^{36}), the
699 100-kyr cycle (in orange; frequency cuts: 0.006667 – 0.01250 cycles/kyr; roll-off rate: 10^{36})
700 and the precession cycle (in blue; frequency cuts: 0.03583 – 0.05417 cycles/kyr; roll-off rate:
701 10^{36}). **F.** 2π -MTM spectrum of the amplitude modulation of the precession cycles. The red and
702 orange curves represent the filter of the 405-kyr and 100-kyr eccentricity, respectively. The
703 405-kyr cycle is filtered with a Taner low-pass filter (frequency cut: 0.004833 cycles/kyr; roll-
704 off rate: 10^{36}). The 100-kyr cycle is filtered with a Taner band-pass filter (frequency cuts:
705 0.006250 – 0.01558 cycles/kyr; roll-off rate: 10^{36}). **G.** 2π -MTM spectrum of the amplitude
706 modulation of the 100-kyr cycle filtered from the amplitude modulation of the precession
707 cycles. The 405-kyr cycle (in red) is filtered using a Taner low-pass filter (frequency cut:
708 0.005417 cycles/kyr; roll-off rate: 10^{36}). **H.** 2π -MTM spectrum of the amplitude modulation of
709 the 100-kyr cycle filtered from the calibrated series. The 405-kyr cycle (in red) is filtered using
710 a Taner low-pass filter (frequency cut: 0.004583 cycles/kyr; roll-off rate: 10^{36}). Note that
711 spectra of panels F to H are obtained with a padding factor of 2.
712



713

714 Fig. 9. Correlations of astronomical time scales in between the Central High Atlas Basin
 715 (Martinez et al., 2017), the Middle Atlas Basin (present study), the Peniche section (Suan et
 716 al., 2008b; Huang and Hesselbo, 2014) and the Yorkshire area (Thibault et al., 2018).